Interactions between comoving magnetic microswimmers

Eric E. Keaveny and Martin R. Maxey
Division of Applied Mathematics, Brown University, 182 George Street, Box F, Providence, Rhode Island 02912, USA
(Received 3 August 2007; revised manuscript received 8 January 2008; published 16 April 2008)

The artificial microswimmer [R. Dreyfus *et al.*, Nature (London) **437**, 862 (2005)] whose mechanism of propulsion is the magnetically driven undulation of a flagellum-like tail composed of chemically linked paramagnetic beads can be used as a physical model with which to study low-Reynolds-number swimming. Understanding how such swimmers interact provides insight into the related problem of quantifying the hydrodynamic interactions between microorganisms. In this study, particle-based numerical simulations are conducted of two comoving artificial swimmers. The resulting swimming speeds are determined over a range of separations for swimmers driven by planar and rotational magnetic fields. The far-field hydrodynamic interactions are analyzed and found to decay as h^{-2} where h is the separation distance. Additionally, the role of the interswimmer magnetic forces is determined.

DOI: 10.1103/PhysRevE.77.041910 PACS number(s): 87.19.rs, 87.16.A−, 87.16.Qp, 87.19.ru

I. INTRODUCTION

From self-organized vortices of two-dimensionally confined sea urchin sperm [1] to millimeter-long trains of wood mouse sperm [2] to turbulence-like structures formed by swarming bacteria [3], the interactions between swimming microorganisms have been observed to lead to a rich variety of collective behaviors. Recent coarse-grained hydrodynamics studies [4] and simulations of rigidly connected point sources [5] and self-locomoting rods [6] lend insight into the instabilities observed in [3]. Additionally, these studies along with [7] established the differences between suspensions of "pusher"-type swimmers where the thrust is generated behind the passive element of the swimmer and "puller"-type swimmers where the thrust is in front of the passive component. As two swimmers approach each other, details concerning the swimmers' kinematics and the near-field hydrodynamic interactions become important [8] and need to be accounted for. Quantifying experimentally the relationship between these dynamics and suspension properties is, in general, quite difficult. The artificial microswimmer [9] offers a controllable model system that may be used in place of microorganisms to provide insight into this relationship. In this case, the differences need to be quantified between this externally driven system and the self-driven swimmer which it mimics.

The artificial swimmer is constructed from a paramagnetic filament tail attached to a human red blood cell. The filament is composed of micron-sized paramagnetic beads linked to each other by flexible DNA molecules. An applied magnetic field is used to drive the motion of the swimmer. By adjusting the frequency and magnitude of the applied field, the kinematics of the swimmer can be altered. Also, by applying different forms of the magnetic field, the device can be made to swim using flagellum beating [9,10] or rotating corkscrew [11] strategies.

As the complexities surrounding the structural details of natural flagella and the uncertainties in specifics of microtubule sliding are not present, accurate theoretical descriptions of the artificial swimmer are available. The dynamics of magnetic filaments and the artificial swimmer have been examined using models where the filament is treated as a continuous elastica subject to magnetic torques and hydrodynamic drag [11–13]. Particle-based methods which consider the motion of individual paramagnetic beads [10,11] provide an alternative description.

Previously [11], we presented and employed a particle-based method where each bead is represented as a rigid paramagnetic sphere and the DNA links are treated as flexible, inextensible rods. We demonstrated the possibility of spiral swimming and identified an optimal range of the parameters governing the swimming speed. We follow this study by now using the particle-based representation to examine the interactions between two microswimmers in comoving configurations. Studying the interactions of artificial microswimmers theoretically provides an example of swimmer-swimmer interactions where the details concerning the driving forces and constitutive laws are well described and differs from studies where the kinematics, rather than the driving forces, of the swimmers are prescribed [14–16]. Additionally, the results presented here allow for the evaluation of the accuracy of theoretical models where the details concerning swimmer propulsion are ignored [4–7]. Interactions of swimmers executing both flagellum beating and rotating corkscrew strategies are considered. The details concerning the nature of the interactions, including the role of the interswimmer magnetic and far-field hydrodynamic forces, are provided. From these results and comparisons with the recent boundary element simulations of a pair of interacting bacteria [8], we may quantify the effectiveness of an externally driven system as a model for an internally driven swimming microorganism.

II. METHODS

A particle-based representation of the artificial swimmer is adopted and described here for a single swimmer. The magnetic filament tail is treated as a series of N rigid spheres. Each sphere $n=1,\ldots,N$ centered at $\mathbf{Y}_n$ has body axes $(\mathbf{t}_n,\mathbf{p}_n,\mathbf{q}_n)$ and represents a paramagnetic bead of radius a and magnetic susceptibility χ. The beads are linked by inextensible, flexible rods of length l, bending modulus κ, and twist modulus C. A large, nonmagnetic sphere of radius R

centered at $\mathbf{Y}_{N+1}$ and having body axes $(\mathbf{t}_{N+1},\mathbf{p}_{N+1},\mathbf{q}_{N+1})$ is tethered to one end of the filament and represents the red blood cell in the experiments.

The Reynolds number associated with the motion of the beads is quite small, $\mathrm{Re}=10^{-5}$, and accordingly, at each instant of time the forces and torques on a bead must sum to zero:

$$\mathbf{F}^n_{hydro}+\mathbf{F}^n_{mag}+\mathbf{F}^n_{elas}=0, \tag{1}$$

$$\boldsymbol{\tau}^n_{hydro}+\boldsymbol{\tau}^n_{elas}=0. \tag{2}$$

A summary of the procedures used to compute these forces and torques is presented here while a complete description may be found in [11].

A. Magnetic interactions

In the experiments, the magnetic susceptibility of the beads is $\chi\approx 1$, and for such a value, the mutually interacting dipole model yields a sufficiently accurate estimate of the interbead magnetic forces. The applied magnetic field and the fields produced by the other beads induce the dipole moment of bead n:

$$\mathbf{m}_n=\frac{4}{3}\pi\chi a_n^3\mathbf{H}_{tot}(\mathbf{Y}_n), \tag{3}$$

where

$$\mathbf{H}_{tot}(\mathbf{Y}_n)=\mathbf{H}(t)+\sum_{q\neq n}\frac{1}{4\pi}\left(\frac{3(\mathbf{Y}_n-\mathbf{Y}_q)(\mathbf{Y}_n-\mathbf{Y}_q)\cdot\mathbf{m}_q}{r_{nq}^5}-\frac{\mathbf{m}_q}{r_{nq}^3}\right), \tag{4}$$

with $r_{nq}=\sqrt{(\mathbf{Y}_n-\mathbf{Y}_q)\cdot(\mathbf{Y}_n-\mathbf{Y}_q)}$. Once the dipole moments are computed, the force on bead n is determined from

$$\mathbf{F}^n_{mag}=\mu_0\nabla_{\mathbf{Y}_n}[\mathbf{m}_n\cdot\mathbf{H}_{tot}(\mathbf{Y}_n)], \tag{5}$$

where μ_0 is the permeability of free space.

B. Elastic coupling

The DNA linkages between the beads are treated as flexible, inextensible rods parametrized by arclength $0\le s\le l$. The shape of each link is governed by a set of linearized beam equations

$$C\frac{d^2\Psi}{ds^2}=0, \tag{6}$$

$$\kappa\frac{d^2\Theta}{ds^2}=\lambda_1\Theta+\lambda_3, \tag{7}$$

$$\kappa\frac{d^2\Phi}{ds^2}=\lambda_1\Phi-\lambda_2, \tag{8}$$

where (Θ,Φ,Ψ) are the Euler angles that vary along the length of the link and relate the body axes of one sphere to that of its neighbor. The values of $(\lambda_1,\lambda_2,\lambda_3)$ are chosen to enforce the constraint of inextensibility, which for the link connecting bead $n-1$ to bead n is

$$(\mathbf{Y}_n-\mathbf{Y}_{n-1})-a_n\mathbf{t}_n-a_{n-1}\mathbf{t}_{n-1}=\int_0^l\mathbf{t}\,ds. \tag{9}$$

The forces and torques on beads $n-1$ and n as a result of the deformation of the link are then

$$\begin{aligned}
\boldsymbol{F}^{n-1}_{elas}&=\lambda_1\mathbf{t}_{n-1}+\lambda_2\mathbf{p}_{n-1}+\lambda_3\mathbf{q}_{n-1},\\
\boldsymbol{F}^{n}_{elas}&=-\boldsymbol{F}^{n-1}_{elas},\\
\boldsymbol{\tau}^{n-1}_{elas}&=\mathbf{M}(0)+a_{n-1}(\mathbf{t}_{n-1}\times\mathbf{F}^{n-1}_{elas}),\\
\boldsymbol{\tau}^{n}_{elas}&=-\mathbf{M}(l)-a_n(\mathbf{t}_n\times\mathbf{F}^{n}_{elas}),
\end{aligned} \tag{10}$$

where

$$\mathbf{M}(s)=\kappa\mathbf{t}\times\frac{d\mathbf{t}}{ds}+C\mathbf{t}\frac{d\Psi}{ds}. \tag{11}$$

C. Hydrodynamic interactions

The hydrodynamic interactions are provided by the force-coupling method (FCM) [17,18]. The particle phase is represented by a body-force distribution in the Stokes equations

$$\nabla p-\eta\nabla^2\mathbf{u}=\sum_{n=1}^{N+1}\mathbf{F}^n_{ext}\Delta_n(\mathbf{x}-\mathbf{Y}_n)+\sum_{n=1}^{N+1}\mathbf{G}^n\cdot\nabla\Xi_n(\mathbf{x}-\mathbf{Y}_n), \tag{12}$$

$$\nabla\cdot\mathbf{u}=0, \tag{13}$$

where

$$\Delta_n(\mathbf{x})=(2\pi\sigma^2_{n,\Delta})^{-3/2}e^{-r^2/2\sigma^2_{n,\Delta}}, \tag{14}$$

$$\Xi_n(\mathbf{x})=(2\pi\sigma^2_{n,\Xi})^{-3/2}e^{-r^2/2\sigma^2_{n,\Xi}}, \tag{15}$$

with $\sigma_{n,\Delta}=a_n/\sqrt{\pi}$, $\sigma_{n,\Xi}=a_n/(6\sqrt{\pi})^{1/3}$, and $\mathbf{F}^n_{ext}=\mathbf{F}^n_{mag}+\mathbf{F}^n_{elas}$. The antisymmetric part of the tensor $\mathbf{G}^n$ is related to the torque on the bead $\frac{1}{2}(G^n_{ij}-G^n_{ji})=\frac{1}{2}\varepsilon_{ijk}\tau^n_{elas,k}$, and the symmetric part is chosen such that

$$\int\frac{1}{2}[\nabla\mathbf{u}+(\nabla\mathbf{u})^{\mathrm{T}}]\Xi_n(\mathbf{x}-\mathbf{Y}_n)d^3\mathbf{x}=0. \tag{16}$$

After computing the resulting flow field, the motion of the particle phase is determined from

$$\mathbf{V}_n=\int\mathbf{u}(\mathbf{x})\Delta_n(\mathbf{x}-\mathbf{Y}_n)d^3\mathbf{x}, \tag{17}$$

$$\boldsymbol{\Omega}_n=\frac{1}{2}\int\boldsymbol{\omega}(\mathbf{x})\Xi_n(\mathbf{x}-\mathbf{Y}_n)d^3\mathbf{x}, \tag{18}$$

where $\boldsymbol{\omega}$ is the vorticity of the fluid.

The FCM has been used successfully in a variety of numerical studies ranging from understanding platelet aggrega-

tion in capillaries [19] to optimizing the performance of colloidal micropumps [20]. The FCM force distribution yields solutions asymptotic to the Stokeslet, rotlet, and stresslet along with the corresponding degenerate multipoles associated with these terms. Additionally, the volume-averaged integration captures the Faxén corrections for particle motion in a spatially varying flow field. In numerical tests, the FCM provided an accurate prediction of the particle mobility for the related problem of a chain of seven particles falling under gravity [21]. Although the FCM does not resolve the lubrication forces between the particles, they may be ignored here as their relative motion is governed exclusively by the elastic coupling.

Once the velocities and angular velocities are determined, the equations of motion for the particle phase,

$$\frac{d\mathbf{Y}_n}{dt} = \mathbf{V}_n, \tag{19}$$

$$\frac{d\mathbf{t}_n}{dt} = \mathbf{\Omega}_n \times \mathbf{t}_n, \tag{20}$$

$$\frac{d\mathbf{p}_n}{dt} = \mathbf{\Omega}_n \times \mathbf{p}_n, \tag{21}$$

$$\frac{d\mathbf{q}_n}{dt} = \mathbf{\Omega}_n \times \mathbf{q}_n, \tag{22}$$

for each bead n are integrated numerically using an explicit, stiffly stable second-order scheme [22]. The values of $(\lambda_1, \lambda_2, \lambda_3)$ for each link are adjusted by a penalty scheme to keep the deviation in length below $1.0 \times 10^{-3} l$.

III. RESULTS

A. Single swimmer

To compare with previous studies, we first perform simulations of an isolated swimmer driven by the magnetic field

$$\mathbf{H} = -H_0(1, h_0 \cos \omega t, 0). \tag{23}$$

In the simulations, the unit of length is taken to be the radius of a paramagnetic bead, a. The length of the linkages is $l = 0.2a$ and corresponds to the length of the DNA molecules binding adjacent beads in the experiments [9]. The filament length is defined as $L = N(2a+l) - l = (2.2N - 0.2)a$. The magnitude of the magnetic field H_0 and the frequency of the magnetic field, ω, are chosen to yield the desired values of the magnetoelastic number

$$M_n = \frac{\pi \mu_0 (\chi a H_0 L)^2}{6K_b(1 - \chi/6)(1 + \chi/12)} \tag{24}$$

and the sperm number

$$S_p = \left(\frac{4\pi \eta \omega L^4}{K_b} \right)^{1/4}. \tag{25}$$

The sperm number gives the ratio of the viscous to elastic forces and provides the ratio of the length of the filament to the elastohydrodynamic length $l_{EH} = (K_b / 4\pi\eta\omega)^{1/4}$ [23]. The elastohydrodynamic penetration length is the characteristic length over which significant bending of the filament will occur. Based on experimental values, real sperm appear to operate at $S_p \approx 7.0$ [24]. The magnetoelastic number describes the ratio of the magnetic forces to elastic forces and provides a relative measure of the driving forces. In the context of microorganisms, such a number would describe the strength of the bending moments produced by microtubule sliding. In the definitions of S_p and M_n, the effective bending modulus of the filament, K_b, is related to the bending modulus of a single link through $K_b = (2a+l)\kappa / l$. These parameters together with the values of h_0, χ, R/L, and C/κ determine the mechanical properties of the swimmer. In all cases considered, $\chi = 1.0$ and $C/\kappa = 1.0$.

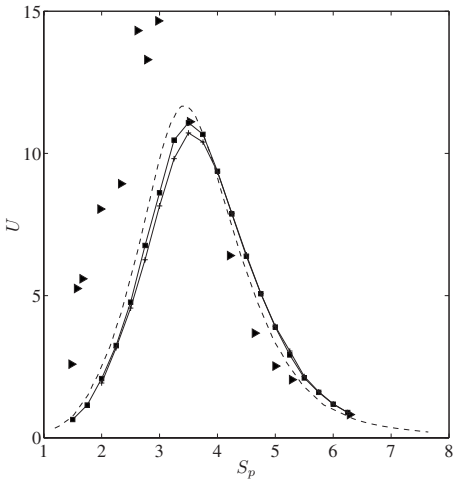

FIG. 1. Scaled swimming speed U of a single swimmer as a function of sperm number S_p. The motion is generated by the magnetic field (23) with $M_n = 16$, $h_0 = 1.16$, and $R/L = 0.129$. The solid line with the square markers shows the scaled swimming speeds obtained using the simulation methods described in Sec. II using only FCM monopoles to resolve the hydrodynamics. The solid line with the crosses was obtained using the full hydrodynamic model. The triangle markers are the experimental results from [9] while the dashed line was obtained by [10].

In the experimental study [9], the scaled swimming speed $U = V/(L\omega)$ of the swimmer was measured over a range of S_p with the values of M_n and h_0 fixed. Figure 1 shows the scaled swimming speed as a function of S_p with $M_n = 16$, $h_0 = 1.16$, and $R/L = 0.129$ as given by the simulation method presented above. At low S_p, the effects of the viscous stresses are minimal and the resulting motion of the swimmer is nearly a rigid rotation. Consequently, the translation of the swimmer is limited. As S_p increases, the deformation of the filament becomes significant and the swimming speed increases. If, however, S_p is too great, the viscous stresses become overwhelming and diminish the amplitude of the deformation and the swimming speed.

The swimming speeds measured by [9] and computed by [10] are also shown in Fig. 1. The swimming speeds given by simulations and those observed in the experiments are comparable, especially at high S_p. The discrepancies between the simulation and experimental results at lower S_p are attrib-

uted to the presence of a nearby surface in the experiments and the deformability and oblate shape of the red blood cell. Such conditions change the drag on the filament and the drag and viscous torque on the tethered body. The hydrodynamic forces and torques have been shown to greatly affect the initial growth of the swimming speed in the context of spiral actuation [11]. The two simulation methods do produce consistent results, although the results found here did not require rescaling as they did in [10].

In addition to the magnetic field (23), the interactions between swimmers driven by the magnetic field

$$\mathbf{H} = -H_0(1, h_0 \cos \omega t, h_0 \sin \omega t) \tag{26}$$

are examined. An extensive study of the artificial swimmer driven by the spiral field is presented in [11].

B. Swimmer-swimmer interactions

The interactions between two comoving artificial microswimmers are examined. We consider four cases where the swimmers are driven by both fields (23) and (26) and in two different configurations. For each configuration, the swimming speed is computed over a range of separations. In the cases considered, $M_n=10$, $S_p=3.0$, and $h_0=1.0$ are fixed and swimming is in the negative x direction. $N=15$ beads comprise the each swimmer's filament tail, giving a length $L=32.8a$. The radius of the tethered sphere is $R=6.0a$, and therefore $R/L=0.183$.

1. Side-by-side configuration

In the first case the separation vector is $\mathbf{r}=(0,0,h)$ and the motion is driven by the planar applied field (23). Here the axis of separation and direction of applied magnetic torque are aligned. Both swimmers have the same scaled swimming speed which is at most 3% less than the single swimmer scaled speed $U_\infty=0.006\,355$. In addition to the motion in the swimming direction, the swimmers move apart from each other along the axis of separation [Figs. 2(a) and 2(b)]. The scaled repulsion speed U_z attains a maximum value of $U_z \approx 0.21U_\infty$ near contact and decays with separation. The motions of the swimmers' tails are synchronized by the applied field and are nearly identical to the beat patterns of the tails of two consecutive planar swimmers considered later on in more detail (Fig. 6).

To analyze the far-field interactions attained when the separation distance is much greater than the length of the swimmer, $h \gg 2R+L+l$, we consider the flow field generated by a low-order expansion of the body-force distribution associated with an isolated swimmer about the position of the tethered sphere, $\mathbf{Y}_{N+1}$ (see the Appendix). As all the interbead forces are equal and opposite, the total force $\Sigma_{n=1}^{N+1}(\mathbf{F}_{mag}^n+\mathbf{F}_{elas}^n)=0$, but the symmetric, $G_{ij}^S(t)$, and antisymmetric, $G_{ij}^A(t)$, parts of the force dipole $G_{ij}^T(t)$ take nonzero values. Taking $\mathbf{x}-\mathbf{Y}_{N+1}=(0,0,h)$, the resulting time-averaged out-of-plane flow according to (A4) is

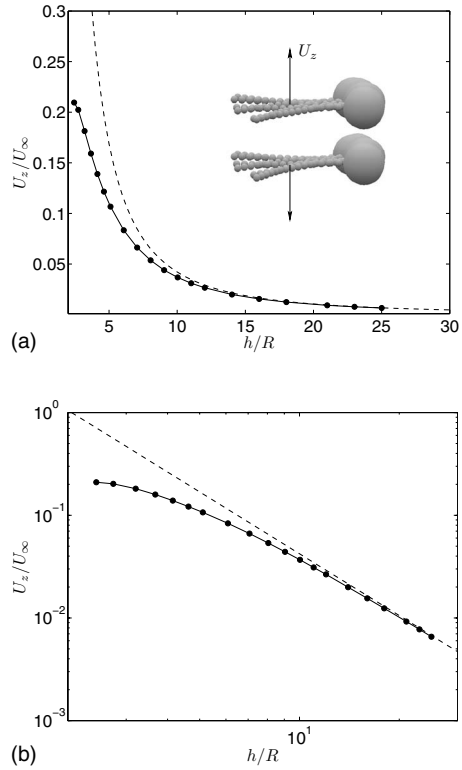

FIG. 2. (a) The repulsion velocity as a function of separation distance for stacked swimmers driven by the applied field (23). (b) Log-log plot of repulsion velocity over a range of separation distances. The dashed lines are provided by (27) which decay as h^{-2}.

$$v_z(h) = -\frac{3\langle G_{33}^S \rangle}{8\pi\eta h^2}, \tag{27}$$

where $\langle G_{33}^S \rangle$ is the nonzero time-averaged value of G_{33}^S. The dashed lines in Figs. 2(a) and 2(b) are provided by (27). At separations $h \geq 1.5(2R+L+l)$, the repulsion speed produced by the simulations does indeed correspond to the far-field disturbance flow produced by the force dipole associated with a single swimmer. This repulsion is a result of the incompressibility of the fluid. Over the course of one period, the motion of the swimmer in the xy plane entrains fluid along the x and y axes which is then forced out along the z axis. The reduction in swimming speed cannot be explained by this analysis as $v_x=0$ since $G_{13}^A=0$ and $x_1-Y_{N+1,1}=0$.

Along with planar swimmers, the interactions of two swimmers driven by the rotating field (26) are considered. The motion of the swimmers over the course of one period is shown in Fig. 3. As before, the separation vector is $\mathbf{r}=(0,0,h)$, but this vector is now perpendicular to the direction of applied torque. Figure 4(a) shows the resulting scaled swimming speed for the spiral swimmers in this configuration. The values are normalized by the isolated value of $U_\infty=0.010\,33$. Again, the two swimmers exhibit the same speed, which is, at any separation, less that the value of an isolated swimmer. As the swimmers come into contact, there is an appreciable decrease in the swimming speed with a near-contact value of $0.8U_\infty$. The swimmers additionally move apart with scaled repulsion speed $U_\parallel$ and precess around each

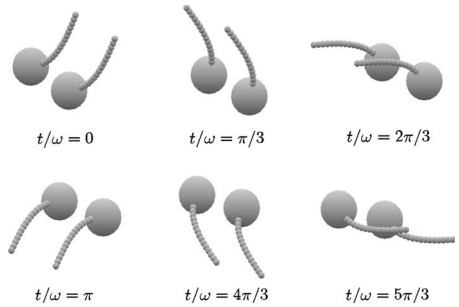

FIG. 3. An end-on view of the motion of two side-by-side spiraling swimmers over one period of the applied field. The motion of the tails is coupled by the applied field that is rotating counterclockwise.

other with precession speed $U_\perp$ [Fig. 4(b)]. These data are shown again in Fig. 5 in a log-log scale.

We compare the present results to those of Ishikawa *et al.* [8] where the trajectories are determined using boundary element simulations for two model bacteria in the same configuration considered here. Initially, as the bacteria swim they precess about each other and the interswimmer separation distance decreases. Over time, however, the bacteria change their swimming directions and swim away from each other. Here, we find that the spiraling artificial microswimmers exhibit precession, but move apart as they swim. This difference in dynamics arises from the model bacteria being

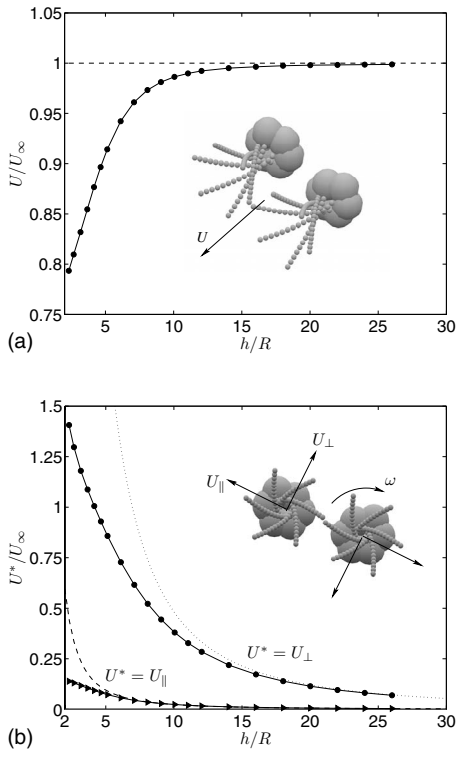

FIG. 4. (a) Swimming speed as a function of separation distance for side-by-side swimmers driven by the applied field (26). (b) Precession velocity $U_\perp$ and repulsion velocity $U_\parallel$ versus separation distance. The dashed and dotted lines are provided by Eqs. (28) and (29), respectively. The insets in the two figures show the motion of the two swimmers over one period of the applied field.

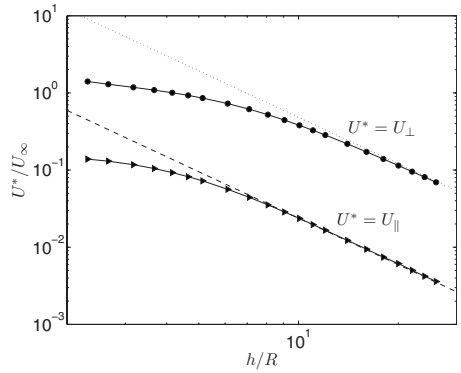

FIG. 5. Log-log plot of the precession and repulsion velocities over a range of separation distances. The dashed is given by (28) and the dotted line by (28). Both decay like h^{-2}.

"pushers" and the artificial swimmers being "pullers." The component of the stresslet related to the repulsion in the artificial swimmer case is the opposite sign of that in the bacterial case. Also, unlike the bacteria, the artificial swimmers will not change their swimming direction since such a reorientation is not be permitted by the applied field.

As before, we may compute the effective force dipole G_{ij}^T for the spiral swimmer and analyze the far-field interactions. With these values of the components of the effective force dipole and (A4) with $\mathbf{x}-\mathbf{Y}_{N+1}=(0,0,h)$, the far-field flow can be determined. The disturbance flow related to the repulsion velocity is

$$v_\parallel(h) = -\frac{3\langle G_{33}^S\rangle}{8\pi\eta h^2}, \tag{28}$$

while the precession velocity is given by

$$v_\perp(h) = -\frac{2G_{23}^A}{8\pi\eta h^2}. \tag{29}$$

The values provided by these equations are shown as dashed and dotted lines in Figs. 4(b) and match the simulation values at large separations. As with the planar swimmer, the far-field repulsion is produced the zz component of the stresslet. The precession is related to the flow generated by the constant external magnetic torque on each swimmer.

2. Consecutive configuration

The resulting swimming speeds for a configuration where the separation vector is $\mathbf{r}=(d,0,0)$ are presented. In this configuration, the swimmers are placed one behind the other. The motion over one period for planar swimmers in this configuration is shown in Fig. 6. For both the planar [Fig. 7(a)] and spiral swimmers, the speed of rear swimmer is greater than the isolated value, while the speed of the front swimmer is less. This effect is limited in the case of spiral actuation where the enhancement in speed of the rear swimmer and the reduction in speed of the front swimmer are at most 5% of the isolated value. For both types of swimmers, the average value of the two speeds for nearly all separations is the value in the isolated case. Figures 7(b) shows the difference in the swimming speeds as a function of separation

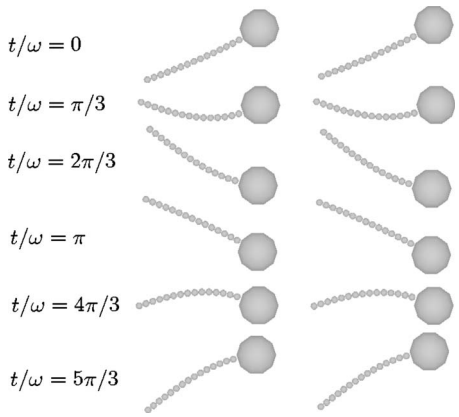

FIG. 6. A top view of the motion of two consecutive planar swimmers over one period of the applied field.

distance for planar swimmers. From (A4) and the components of G^T_{ij}, the far-field disturbance flow corresponding this interaction is

$$v(d) = -\frac{3\langle G^S_{11}\rangle}{8\pi\eta h^2}. \tag{30}$$

The differences in speeds are provided by twice the absolute value of (30) and are shown as the dashed lines in Figs. 7(b). The far-field values are attained at separations of approximately two and a half swimmer lengths. Also, the symmetry

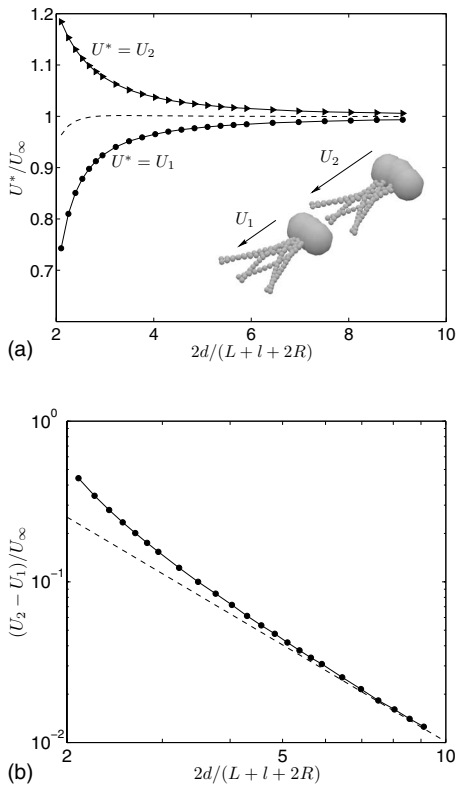

FIG. 7. (a) Swimming speeds for two swimmers arranged consecutively and driven by applied field (23). (b) Log-log plot of the difference in swimming speeds with the dashed line being from 30 with the value of $\langle G^S_{11}\rangle$ for the planar swimmer.

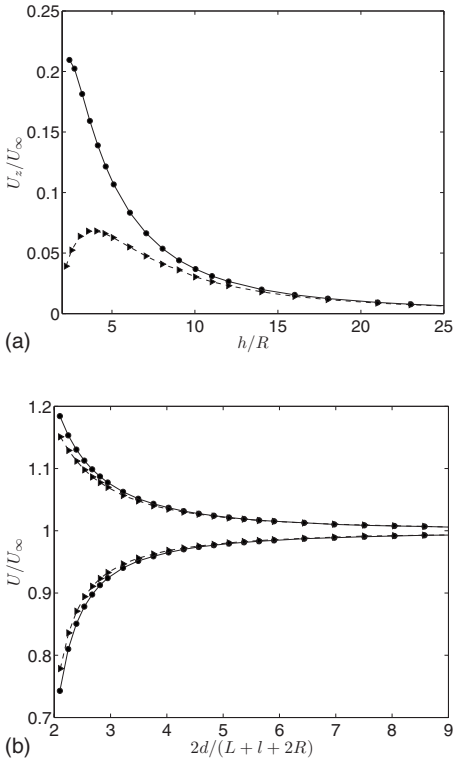

FIG. 8. (a) The repulsion velocity as a function of separation. (b) The two swimming speeds for consecutive planar swimmers. The solid line with the circular markers is from simulations where the magnetic interactions are included while the dashed line with the triangular markers corresponds to the simulations where the magnetic interactions are ignored.

of the interaction is evident as the far-field interaction illustrates $U_1(d) = U_\infty - |v(d)|/(L\omega)$ and $U_2(d) = U_\infty + |v(d)|/(L\omega)$.

C. Interswimmer magnetic interactions

Along with the hydrodynamic interactions already discussed, interswimmer magnetic forces are present and affect the resulting dynamics. The magnetic interactions are akin to those that arise between self-assembled chains in suspensions of paramagnetic beads [25]. To quantify their effect, we conduct simulations where the interswimmer magnetic interactions are ignored. As the resulting motions are modified by hydrodynamic interactions alone, when compared to the motions from the full simulations the importance of the magnetic interactions can be ascertained. This comparison is done for planar swimmers in the stacked and consecutive configurations.

Figures 8(a) shows the repulsion velocity for the stacked configuration. The near-contact repulsion velocity, however, is clearly dependent upon the lateral magnetic interactions. As the separation increases, the magnetic interactions decay rapidly and the far-field hydrodynamics dominate the dynamics. The slight decrease in swimming speed found for planar swimmers in this configuration was not affected by the removal of the magnetic interactions. For swimmers in the consecutive configuration, the magnetic attraction between the filaments does enhance the speed of the rear swim-

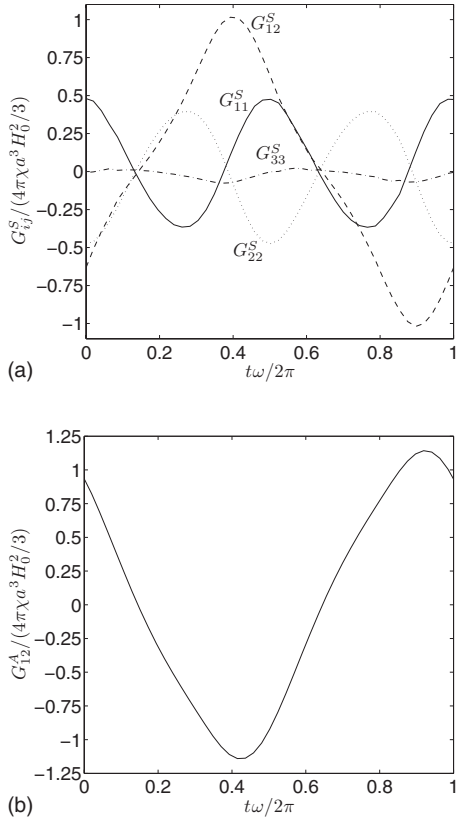

FIG. 9. Components of the force dipole of the planar swimmer: (a) The nonzero components of the traceless stresslet G^S_{ij} over the course of one period on the applied field. (b) The nonzero component of the antisymmetric part of the force dipole, G^A_{12}.

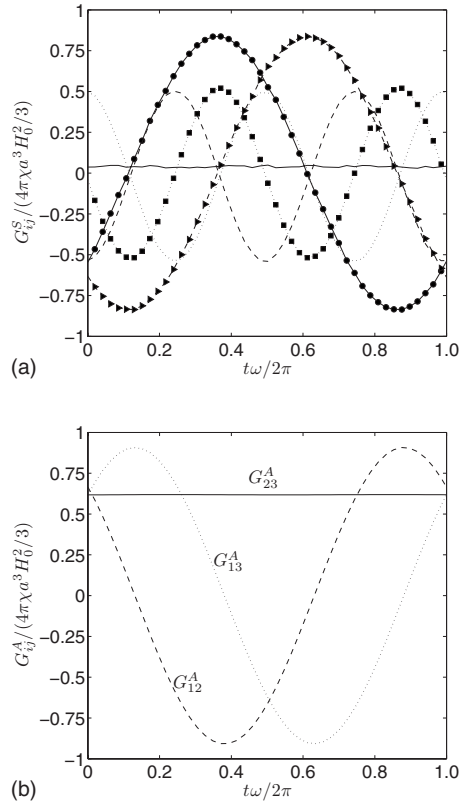

FIG. 10. Components of the force dipole of the spiral swimmer: (a) The nonzero components of the traceless stresslet G^S_{ij} over the course of one period on the applied field. The lines without the markers show to diagonal components with the solid line being G^S_{11}, the dashed line G^S_{22} and the dotted line G^S_{33}. The lines with the markers are the off-diagonal components where the solid line with circular markers is G^S_{12}, the dashed line with triangular markers is G^S_{13}, and the dotted line with the square markers is G^S_{23}. (b) The nonzero component of the antisymmetric part of the force dipole, G^A_{12}, G^A_{13}, and G^A_{23}.

mer while hindering that of the front swimmer. This enhancement, however, is modest, and the hydrodynamics appear to dominate, even at small separations.

IV. SUMMARY AND CONCLUSIONS

In this study, a particle-based method was used to conduct simulations of the artificial microswimmer. This particle-based method treated the magnetic swimmer as a series of rigid spheres connected by inextensible flexible rods. The magnetic forces were treated using a point-dipole approach, and the interbead hydrodynamic interactions were provided by the FCM. First, simulations of a single swimmer were conducted. The resulting swimming speeds were consistent with previous simulations and compared favorably with the experiments at high S_p. The effects of a nearby surface need to be included in order to match the low-S_p experimental results. Simulations of two comoving artificial swimmers are performed. Cases are considered where the swimmers are driven by both planar and rotary fields in two different configurations. For the values of M_n, S_p, and h_0 used in these simulations, the resulting scaled swimming speed for a single swimmer was $U=0.006\,355$ for planar actuation and $U=0.010\,33$ for spiral actuation. These values fall within the range of scaled swimming speeds of microorganisms which, for example, are $U=0.0033$ for *E. Coli* bacteria [26], $U=0.012$ for bull sperm, and $U=0.0253$ for sea urchin sperm [27]. For the side-by-side, or stacked, configurations, the swimming speed is the same for each swimmer and less than the value for an isolated swimmer. The reduction in speed is greater for the spiral-type swimmers. In addition to motion in the swimming direction, the swimmers move apart from each other and the spiral swimmers also precess around each other. At large separations, the interactions decay like h^{-2} according to the far-field disturbance flow produced by a swimmer. Consecutive swimmers move only in the swimming direction, but the rear swimmer moves faster, while the front swimmer is slower. Again the interaction at large separations is provided by the force dipole associated with the swimmers. To understand the role of the magnetic interactions, simulations were conducted where the interswimmer magnetic forces were not included. By comparing these results to those from the full simulations, it is found that only the near-field repulsion for stacked swimmers is significantly effected by the magnetic forces.

Although the dynamics and interactions of this novel device are of interest in their own right, the results indicate that the interactions between the externally driven artificial mi-

croswimmer resemble the interactions between swimming microorganisms. For example, since the magnetic field exerts no net force on a swimmer the far-field hydrodynamic interactions decay as h^{-2} which is what one expects between two force-free and torque-free self-driven swimmers. Based on the results presented here, it is therefore reasonable to assume that at greater than separations of around two swimmer lengths, the far-field hydrodynamics will also provide a good approximation of the hydrodynamic interactions between microorganisms. Additionally, these results encourage the understanding of how the artificial swimmer behaves near a rigid surface and relates to the motion of microorganisms near surfaces [28]. By comparing with simulations of model bacteria [8], we see that suspensions of artificial microswimmers will not exhibit reorientation or dramatic changes in wave motion as a result of the hydrodynamic interactions. These limitations restrict the possibility of studying more generally phenomena such as the bacterial turbulence [3] or the formation of sperm vortices [1] with artificial swimmers.

ACKNOWLEDGMENTS

This work was supported by the National Science Foundation under Grant No. CTS-0326702.

APPENDIX

To analyze the far-field interactions attained when the separation distance is much greater than the length of the swimmer, $h \gg 2R+L+l$, we consider the flow field generated by a low-order expansion of the body-force distribution associated with an isolated swimmer about the position of the tethered sphere, $\mathbf{Y}_{N+1}$:

$$\sum_{n=1}^{N+1} F_i^n \delta(\mathbf{x}-\mathbf{Y}_n) + \sum_{n=1}^{N+1} G_{ij}^n \frac{\partial \delta(\mathbf{x}-\mathbf{Y}_n)}{\partial x_j} \approx \left(\sum_{n=1}^{N+1} F_i^n \right) \delta(\mathbf{x}-\mathbf{Y}_{N+1}) + \left(\sum_{n=1}^{N+1} G_{ij}^n + F_i^n (\mathbf{Y}_{N+1}-\mathbf{Y}_n)_j \right) \frac{\partial \delta(\mathbf{x}-\mathbf{Y}_{N+1})}{\partial x_j}. \tag{A1}$$

Since both the interbead magnetic and elastic forces are equal and opposite, the total force acting on the swimmer at any instant in time is zero, $\Sigma_{n=1}^{N+1} \mathbf{F}^n = \mathbf{0}$. The moments of the forces and the force dipoles, however, are nonzero and provide the leading-order contribution to the flow. Defining $G_{ij}^T = \Sigma_{n=1}^{N+1} G_{ij}^n + F_i^n (\mathbf{Y}_{N+1}-\mathbf{Y}_n)_j$ and decomposing this tensor into its traceless, symmetric part (the stresslet)

$$G_{ij}^S = \frac{1}{2}(G_{ij}^T + G_{ji}^T) - \frac{1}{3} G_{kk}^T \delta_{ij} \tag{A2}$$

and its antisymmetric part

$$G_{ij}^A = \frac{1}{2}(G_{ij}^T - G_{ji}^T), \tag{A3}$$

the leading-order flow field is, in index notation, given by

$$v_i(\mathbf{x}-\mathbf{Y}_{N+1}) = \frac{1}{8\pi\eta} \left(-2 \frac{(\mathbf{x}-\mathbf{Y}_{N+1})_j}{r^3} G_{ij}^A - \frac{3(\mathbf{x}-\mathbf{Y}_{N+1})_i (\mathbf{x}-\mathbf{Y}_{N+1})_j (\mathbf{x}-\mathbf{Y}_{N+1})_k}{r^5} G_{jk}^S \right), \tag{A4}$$

where $r = \sqrt{(\mathbf{x}-\mathbf{Y}_{N+1}) \cdot (\mathbf{x}-\mathbf{Y}_{N+1})}$. For the planar swimmer, the four nonzero components of the symmetric part over one period are shown in Fig. 9(a) and the nonzero component of the antisymmetic part is presented in Fig. 9(a). Figure 10(a) shows the components of G_{ij}^S, and Fig. 10(b) shows the components of G_{ij}^A for the spiral case. Here, the constant value G_{23}^A indicates the time-independent torque on the swimmer produced by the applied field.

[1] I. H. Riedel, K. Kruse, and J. Howard, Science **309**, 300 (2005).
[2] H. Moore, K. Dvorakova, and W. Breed, Nature (London) **418**, 174 (2002).
[3] C. Dombrowski, L. Cisneros, S. Chatkaew, R. E. Goldstein, and J. O. Kessler, Phys. Rev. Lett. **93**, 098103 (2004).
[4] R. A. Simha and S. Ramaswamy, Phys. Rev. Lett. **89**, 058101 (2002).
[5] J. P. Hernandez-Ortiz, C. G. Stoltz, and M. D. Graham, Phys. Rev. Lett. **95**, 204501 (2005).
[6] D. Saintillan and M. J. Shelley, Phys. Rev. Lett. **99**, 058102 (2007).
[7] T. Ishikawa, M. P. Simmonds, and T. J. Pedley, J. Fluid Mech. **568**, 119 (2006).
[8] T. Ishikawa, G. Sekiya, Y. Imai, and T. Yamaguchi, Biophys. J. **93**, 2217 (2007).
[9] R. Dreyfus, J. Baudry, M. L. Roper, M. Fermigier, H. A. Stone, and J. Bibette, Nature (London) **437**, 862 (2005).
[10] E. Gauger and H. Stark, Phys. Rev. E **74**, 021907 (2006).
[11] E. E. Keaveny and M. R. Maxey, J. Fluid Mech. **598**, 293 (2008).
[12] M. Roper, R. Dreyfus, J. Baudry, M. Fermigier, J. Bibette, and H. A. Stone, J. Fluid Mech. **554**, 167 (2006).
[13] A. Cebers and I. Javaitis, Phys. Rev. E **70**, 021404 (2004).
[14] G. I. Taylor, Proc. R. Soc. London, Ser. A **209**, 447 (1951).
[15] M. Ramia, D. L. Tullock, and N. Phan-Thien, Biophys. J. **65**,

755 (1993).
[16] L. J. Fauci and A. McDonald, Bull. Math. Biol. **57**, 679 (1995).
[17] M. R. Maxey and B. K. Patel, Int. J. Multiphase Flow **27**, 1603 (2001).
[18] S. Lomholt and M. R. Maxey, J. Comput. Phys. **184**, 381 (2003).
[19] I. V. Pivkin, P. D. Richardson, and G. E. Karniadakis, Proc. Natl. Acad. Sci. U.S.A. **103**, 17164 (2006).
[20] D. Liu, M. R. Maxey, and G. E. Karniadakis, J. Micromech. Microeng. **14**, 567 (2004).
[21] S. L. Dance and M. R. Maxey, J. Comput. Phys. **189**, 212 (2003).
[22] G. E. Karniadakis, M. Israeli, and S. A. Orszag, J. Comput. Phys. **97**, 414 (1991).
[23] C. H. Wiggins and R. E. Goldstein, Phys. Rev. Lett. **80**, 3879 (1998).
[24] C. P. Lowe, Philos. Trans. R. Soc. London, Ser. B **358**, 1543 (2003).
[25] E. M. Furst and A. P. Gast, Phys. Rev. E **62**, 6916 (2000).
[26] S. Chattopadhyay, R. Moldovan, C. Yeung, and X. L. Yu, Proc. Natl. Acad. Sci. U.S.A. **103**, 13712 (2006).
[27] C. Brennen and H. Winet, Annu. Rev. Fluid Mech. **9**, 339 (1977).
[28] E. Lauga, W. R. DiLuzio, G. M. Whitesides, and H. A. Stone, Biophys. J. **90**, 400 (2006).